Effects of Grain Size on the Thermoelectric Properties of Cu2SnS 3 : An Experimental and First-Principles Study

Ketan Lohani, Himanshu Nautiyal, Narges Ataollahi, Krishnendu Maji, Emmanuel Guilmeau, Paolo Scardi

To cite this version:

Ketan Lohani, Himanshu Nautiyal, Narges Ataollahi, Krishnendu Maji, Emmanuel Guilmeau, et al.. Effects of Grain Size on the Thermoelectric Properties of Cu2SnS 3 : An Experimental and First-Principles Study. ACS Applied Energy Materials, 2021, 4 (11), pp.12604-12612. 10.1021/acsaem.1c02377 . hal-03854032

HAL Id: hal-03854032
https://hal.science/hal-03854032v1

Submitted on 16 Nov 2022

Effects of grain size on the thermoelectric properties of Cu_2SnS_3 (CTS): An experimental and first-principles study

Ketan Lohani[1], Himanshu Nautiyal[1], Narges Ataollahi[1], Krishnendu Maji,[2] Emmanuel Guilmeau[2], & Paolo Scardi[1]**

[1]Department of Civil, Environmental & Mechanical Engineering, University of Trento, Via Mesiano 77, 38123, Trento, Italy

[2]CRISMAT, CNRS, Normandie Univ, ENSICAEN, UNICAEN, 14000 Caen, France

Abstract:

Cu-Sn-based sulfides are earth-abundant and non-toxic compounds, of special interest for low-cost energy harvesting applications. In the present work, we have investigated the effect of grain-size on the thermoelectric properties of Cu_2SnS_3 (CTS). Three dense CTS samples with nanometric grains were produced by mechanical-alloying combined with Spark Plasma Sintering, preserving the small size of crystalline domains to 12 nm, 25 nm, and 37 nm, respectively. The experimental results show that the Seebeck coefficient (S) and electrical resistivity (ρ) decrease with decreasing domain sizes, while the thermal conductivity (κ) increases. A smaller domain size correlates with a lower resistivity and a degenerate semiconductor-like behaviour due to higher carrier concentration. At the same time, our synthesis method leads to materials with very low lattice thermal conductivity thanks to the nanometric size of grains and structural disorder. As a result, the sample with the smallest grain size exhibits the highest zT of ~0.4 at 650 K. First-principles Density Functional Theory (DFT) simulations on various CTS crystallite surfaces revealed localized states near the Fermi level and the absence of bandgap, indicating the metallic nature of the surfaces. Various CTS systems were tested by DFT, showing the following order of increasing formation energy: stoichiometric CTS, Cu-vacancy, Cu-rich, Sn-vacancy, and Sn-rich.

Keywords: Cu_2SnS_3, grain size effect, DFT, thermoelectric Cu_2SnS_3, spark plasma sintering, *p*-type semiconductor.

Introduction:

Most commercially available thermoelectric (TE) devices use toxic and scarce materials, making them expensive and potentially hazardous, e.g., Sb_2Te_3, Bi_2Te_3, etc. In recent years, the search for high-performance, non-toxic, eco-friendly, and earth-abundant TE materials has led to the exploration of multinary sulfides.[1,2] Chalcogenides[3], colusites[4,5], and other metal-based sulfides[6–8] could be viable alternatives to existing materials.[9] Cu-based sulfides have low formation energy, so that it is possible to produce them by short-period reactive milling using a planetary or vibrating mill. As also shown in the present work, high-energy reactive ball-milling, also called mechanical-alloying, can be employed with success to synthesize new and disordered phases. In addition, milling offers the advantage of facile and scalable production for industrial use.[10]

The energy conversion efficiency of a TE material is determined by a dimensionless figure of merit (zT) expressed as $zT=S^2/\rho\kappa{*}T$, where S, ρ, κ, and T are Seebeck coefficient, electrical resistivity, thermal conductivity, and absolute temperature, respectively. S^2/ρ is referred to as power factor (PF). The Seebeck coefficient and electrical resistivity are strongly dependent of the carrier concentration (n), mobility (μ), and effective mass of the charge carriers (m^*), (see Equations 1 and 2 below). A low carrier concentration and high effective mass of charge carriers can increase the Seebeck coefficient, but it also penalizes the electrical conductivity and vice versa.[1,11]

$$S = Am^*\left(\frac{\pi}{3n}\right)^{\frac{2}{3}}T \qquad -1$$

$$\sigma = ne\mu \qquad -2$$

$$\kappa_e = \frac{LT}{\rho} \qquad -3$$

where A, e, and L represent a constant, charge of an electron, and Lorenz number, respectively.

Besides high *PF*, TE materials also require low thermal conductivity (κ), composed of a lattice (κ_l) and an electronic contribution (κ_e), combined as: $\kappa = \kappa_l + \kappa_e$. The lattice contribution can be decreased by increasing the grain boundary density, vacancies, defects, impurities, strain, etc. Differently, κ_e shows a strong dependence on the electrical resistivity, as in the Wiedemann-Franz law (see equation 3).[5] More recently, the determination of the thermoelectric quality factor (β) given by $\beta = \mu_0 m_{dos}{}^{*3/2}/\kappa_l$ (where μ_0 and $m_{dos}{}^*$ are the non-degenerate mobility and density of state effective mass, respectively) is in practice for the simultaneous optimization of all TE parameters.[12,13]

$Cu_{2+x}Sn_{1-x}S_3$ (CTS) polymorphs are used in many applications such as photovoltaics, transistors, LEDs, and thermoelectric materials. A recent study has also suggested a potential use of CTS quantum dots for photodetector applications.[14] CTS polymorphs have been extensively studied as *p*-type thermoelectric materials showing moderately high *PF* with high or low thermal conductivity, depending whether the crystal structure is ordered or disordered.[15–17] To increase the thermoelectric performance, different cationic substitutions have been investigated with the aim to tune the carrier concentration and to introduce structural disorder. Among the various studies, Zhao *et al.* have reported the highest zT ~0.9 (at T > 700 K) so far, by simultaneous cobalt and antimony doping.[18]

Zhai *et al.*[19] and Shigemi *et al.*[20] have shown that the hybridization of Cu-3*d* and S-3*p* orbitals in the valence band (VB) is responsible for the *p*-type nature of CTS. Heavy acceptor-doping due to unfilled *d*-orbitals of Co[21], Cu[22], Ni[18], Fe[23], and Mn[24] enhance the DOS effective mass of carriers (holes) and electrical conductivity, resulting in a high *PF* ~10 μW/cm K^2, around 700 K. Cationic substitution also transforms the CTS crystal structure from ordered (monoclinic *Cc*)[25] to tetragonal I-*42*m[26] and disordered (cubic: *F-43m*).[15] In most of the cases, a mixture of the different phases is obtained. Deng *et al.*[22] have shown the influence of Cu/Sn ratio in $Cu_{2+x}Sn_{1-x}S_3$ on the electrical and thermal properties. More recently, V. Pavan Kumar *et al.*[17] have discovered a new ordered monoclinic structure $Cu_5Sn_2S_7$ by increasing the Cu/Sn ratio up to $x = 0.15$ leading to a specific ordering of Cu and Sn in the structure. In summary, the hole doping in CTS compounds, induced by the substitution of Cu, Sn or S by aliovalent cations, or by Cu for Sn substitution, increases the carrier concentration. Disordering phenomena, usually induced by the cationic/anionic substitution, scatters the phonon waves more effectively, resulting in a higher TE figure of merit.

The disordered cubic CTS and Cu_2SnSe_3 (CTSe) phases can also be produced and stabilized without chemical alteration.[16,27,28] The optical absorption measurements revealed a lower bandgap for the disordered CTS/Se polymorphs. The lower bandgap enhances the carrier concentration resulting in a higher PF compared to its ordered polymorph. Furthermore, in a theoretical study, Baranowski *et al.* [29] have also reported band tailing and mid-gap states for the disordered CTS phase. The structural disorder introduces potential energy fluctuations in the lattice that allow energy levels within the forbidden gap, responsible for the band tailing and reduced band gap.[27,29] Moreover, Dahule *et al.*[30] have studied the electronic structure properties of (200) and (-131) surfaces of monoclinic CTS and shown their metallic character. It is worth mentioning that the metallic character was confirmed using different potentials, including the Heyd-Scuseria-Ernzerhof (HSE) potential, which results in a better estimation of the bandgap.

In terms of synthesis, the literature suggests a three-step top-down approach to produce CTS samples for TE applications. First, CTS is produced from the elemental powders (Cu, Sn, S, and dopant elements) using an extended high-temperature solid-state reaction.[11] In the second step, the grain size is sometimes reduced by ball-milling. Finally, high-density pellets are produced using spark-plasma-sintering or hot-pressing. This approach results in highly crystalline materials with average domain sizes ranging from half to several microns. This synthesis method requires a long annealing time at high temperatures, which is time and resource-consuming.

Alternatively, CTS compounds, as many other Cu-based sulphides, can be produced by combined high-energy reactive ball-milling (mechanical alloying) and Spark Plasma Sintering (SPS) or hot pressing.[17,31] Mechanical alloying allows to produce fine, homogeneous, pre-crystallised and highly reactive powders, which usually lead to high purity, crystallinity and dense samples after sintering with small grain and crystallite sizes. Furthermore, a highly dense disordered CTS polymorph can be stabilized without any chemical substitution.[10]

The present work aims to shed light on the degenerate semiconductor-like behaviour of nanocrystalline CTS samples. Three dense CTS samples were produced using powder synthesized by high-energy reactive ball milling and SPS. We have investigated the effects of grain size on the thermoelectric properties. Structural and microstructural analyses suggested a stoichiometry deviation in CTS phases sintered at low temperature, together with a very small crystallite and grain size. *Ab initio* calculations using Density Functional Theory (DFT) indicated the metallic nature of CTS surfaces, leading to a degenerate semiconductor-like trend with temperature. Further evidence is presented on the formation energies for various CTS systems with vacancies and chemical deviations.

Materials and methods:

Experimental: Elemental powders (Cu, Sn, and S) were weighted in stochiometric ratio and fed in WC vials with WC balls. A Fritsch Pulverisette-4 mill was operated for 1h, producing ~6 g of as-milled CTS powder. The entire production process was performed in a glove box with argon filled environment. During the milling, no lubricant was introduced to avoid any contamination. The production of CTS powder by high-energy ball milling of elemental powders and binary sulfides is discussed in detail elsewhere.[16,27]

The as-milled powder was sintered using a Spark Plasma Sintering (SPS) machine (FCT HPD 25) at various temperatures and pressures to optimize the sintering conditions (Table 1). Relative density of the samples is 86, 96, and 94% for sample A, B and C, respectively.

Structural analysis was performed using X-Ray Diffraction (XRD). XRD data were collected in θ/2θ Bragg-Brentano geometry using a Panalytical Xpert Pro diffractometer equipped with Cu-$K\alpha$ ($\lambda=1.5406$ Å) source. Micrographs and Electron Dispersive X-ray (EDX) spectroscopy analyses were collected using a JEOL JSM 7200F scanning electron microscope equipped with EDX X-Flash Bruker detector.

The electrical resistivity (ρ) and Seebeck coefficient (S) were measured simultaneously from 300 K up to 700 K on bar-shaped samples of typical dimensions 2×3×10 mm^3 using an ULVAC-ZEM3 instrument under partial helium pressure. A NETZSCH LFA-457 apparatus was used for measuring the thermal diffusivity under argon flow. The thermal conductivity (κ) was determined as the product of the geometrical density, the thermal diffusivity, and the theoretical heat capacity using the Dulong−Petit approximation. The lattice contribution to the thermal conductivity (κ_l) was determined by subtracting the estimated electronic component (κ_e) from the measured total thermal conductivity, κ. The measurement uncertainties are estimated to be 6% for the Seebeck coefficient, 8% for the electrical resistivity, 11% for the thermal conductivity, and 16% for the final dimensionless figure of merit.

Hall effect measurements at RT were carried out using a Physical Properties Measurement System (PPMS; Quantum Design) under an applied magnetic field of 9 T.

Computational:

The electronic structure calculations were performed using DFT as implemented in Vienna *ab initio* Simulation Package.[32,33] The interaction between electrons and ions was described using the Projector-Augmented-Wave (PAW) method. The Generalized Gradient Approximation (GGA) with Perdew-Burke-Ernzerhof (PBE)[34] electron exchange-correlation was used for the calculations.

We have performed the calculations for (001), (010), and (100) slabs of monoclinic CTS, and two disordered CTS cells with sulfur termination. We considered two cases for the disordered cell, one with the Cu-rich and the other with Sn-rich atomic layer below the terminating sulfur layer. For all the calculation CTS stoichiometry was preserved. A vacuum of 15 Å was created to minimize the interaction between the periodic copies. In the disordered cells, the atoms of the lower four layers were fixed in position, whereas the atoms of the upper four layers were free to move. Relaxation was performed with a plane-wave kinetic energy cut-off and an electronic convergence of 350 eV and 10^{-5} eV, respectively. The involvement of core electrons was seized by freezing. Only $3d^{10}4s^1$, $4d^{10}\ 5s^2\ 5p^2$, and $3s^2\ 3p^4$ electrons were treated as valence electrons for Cu, Sn and S, respectively. The cell parameters were fixed, whereas the atomic position was allowed to change for relaxation. The electronic convergence was set to 10^{-6} eV for DOS calculations. Brillion zone sampling was performed on a k-point grid of 9×9×1 and 5×5×1 for monoclinic slabs and disordered cells, respectively. The k-mesh was reduced for the disordered cell due to its larger size.

The formation energy calculations were performed on Cu-rich, Cu-vacant, Sn-rich, and Sn-vacant cells. For these calculations, the plane wave kinetic energy cut-off and electronic convergence were changed to 400 eV and 10^{-6} eV, respectively. A Monkhorst-Pack[35] k-point mesh of 7×7×7 (centered at the gamma point) was used to integrate the Brillion zone. One atom was removed from the supercell, and the remaining atoms were allowed to relax for the vacancy calculations. The off-stoichiometry calculations were performed on a supercell of 72 atoms with stable monoclinic phase, where one Cu atom was replaced by one Sn atom and vice versa, respectively for the Sn-rich and Cu-rich simulations.

Results and discussion:

XRD patterns collected on as-milled powder with increasing milling times are shown in Figure 1. Due to its low formation energy, short milling of 15 min led to the formation of binary sulfides, especially CuS. As the milling time was increased to 30 min, the appearance of diffraction peaks of sphalerite-type structure can be noticed. However, unreacted SnS and Sn powder were still present in the sample. With the further increase of milling time to 1 h, the as-milled powder showed four broad diffraction peaks, implying the formation of a sphalerite-type crystal structure. It is worth mentioning here that, among all the elements, Sn incorporated last in the CTS system. Broad Bragg-peaks with diffuse backgrounds imply that the one-hour milled powder consists of low crystalline CTS grains with a small domain size.

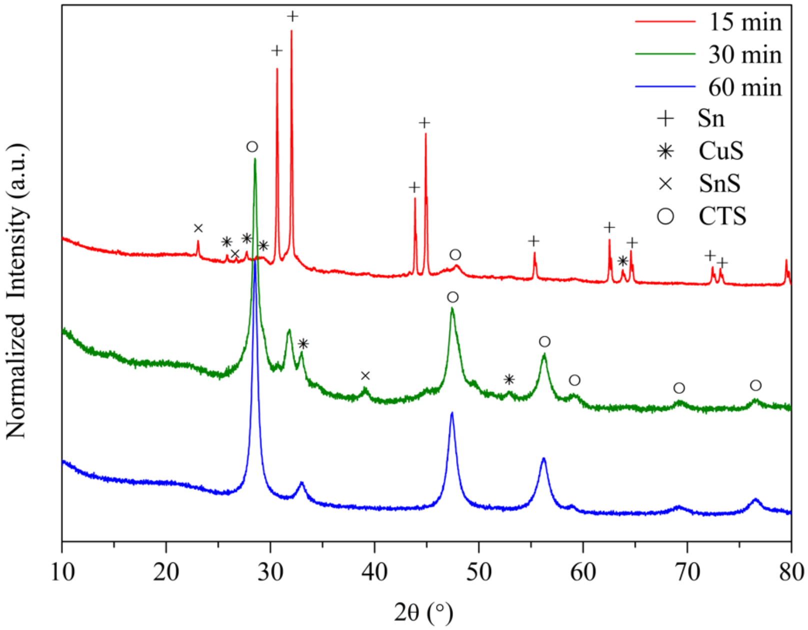

Figure 1. XRD patterns for the powder milled for 15, 30, and 60 min.

SEM-EDX data collected on 60 min milled powder at full-frame image showed the presence of stoichiometric CTS. On the same sample, various micrographs and EDX data were collected in different magnifications from different parts of the SEM grid. It indicated that the as-milled powder has a non-homogeneous chemical distribution with a small domain size, which tend to agglomerate in larger particles (Figure S1).

High-density bulk CTS samples were produced by SPS under different sintering conditions (listed in Table. 1). Sintered samples maintained the same Bragg-peak positions as the as-milled powder. However, sharper Bragg peaks for sintered samples indicate an increased crystallinity and crystallite size. XRD line profile analysis was performed by the Rietveld method[36] using Topas 7 software[37]. We employed the Whole Powder Pattern Modelling (WPPM) macro[38] to simulate the peak profile. The instrumental profile was obtained from a LaB_6 standard sample.[39]A nine-point Chebyshev polynomial and a *1/x*-function were used to simulate the background and low-angle intensity, respectively. Subsequently, zero shift and other parameters were systematically refined[40]. During the refinement, the variation of the Debye-Waller coefficients (thermal factors) was restricted between 0 to 2 for all atoms. For all the samples discussed below, the goodness of fit (*gof*) was ~1.1-1.3.

Disordered CTS has a Zinc-blende (ZnS) like (cubic) close-packed face centered structure, which arranges its atoms in the *F-43m* (216) space group. The *4a* Wyckoff position is occupied by Cu and Sn atoms with occupancy 2/3 and 1/3, respectively, while the *4c* site is occupied by S atoms with occupancy 1. The lattice parameter, phase density, and cell volume determined from Rietveld refinement were 5.43 Å, 4.71 g/cm^3, and 160.50 Å^3, respectively. No microstrain was observed for any sample. Average domain size and the weight fraction of CTS and secondary phases are listed in table 1 for the different sintering conditions. All the samples showed disordered cubic CTS structures. However, a small amount (weight fraction <0.5%) of SnO_2 was observed for samples A and C. For sample B (see figure 2a), two Bragg peaks around $2\theta \sim$ 16° and ~31° were observed. Sample B may have a small amount of monoclinic phase. But the two peaks are quite broad which makes it hard to quantify the monoclinic phase reliably, and it is certainly below 1% in weight.

The size of crystalline domains was estimated as 12±10 nm, 25±10 nm, and 37±10 nm for samples A, B, and C, respectively. The reported average grain size for high-density CTS samples prepared by the three-step method (discussed in the introduction) is in the range of 500-600 nm,[26] and in some cases, micron-size grains are also reported.[21] In contrast, traditionally sintered samples (without applying pressure) showed smaller grains, domain size ranging from ~50 nm to a few 100 nm, and low density.[16] The mechanical-alloying combined with SPS method proposed here constrained the grain size below 50 nm,[31] while promoting densification at relatively low sintering temperature.

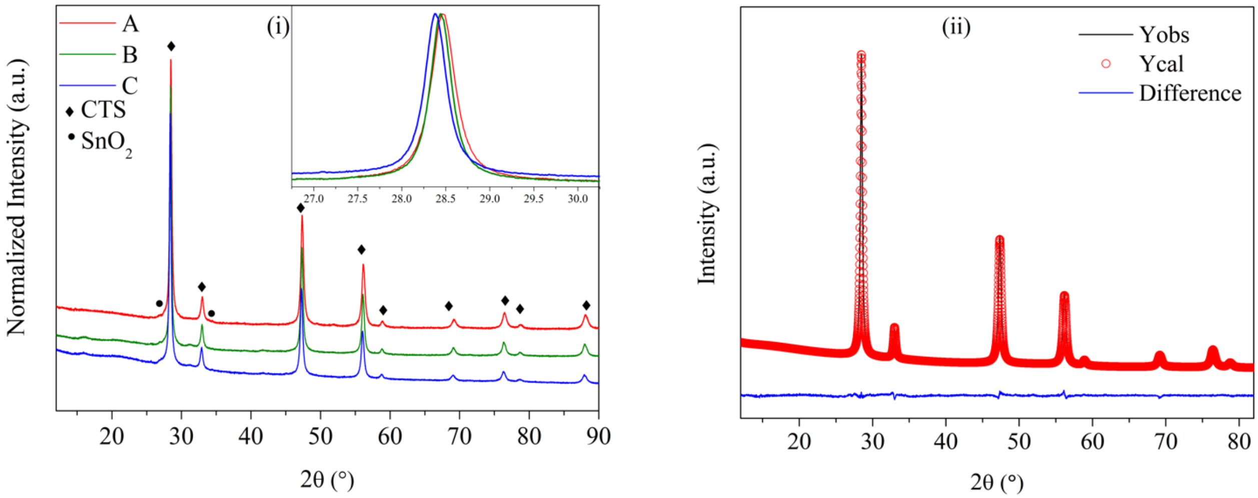

Figure 2. (i) XRD pattern of samples sintered on various conditions.; (ii) Riet1veld refinement data for Sample A (collected (*Yobs*), calculated (*Ycal*), difference (*Difference*) pattern. See Figure S2 for the Rietveld refinement data for samples B and C.

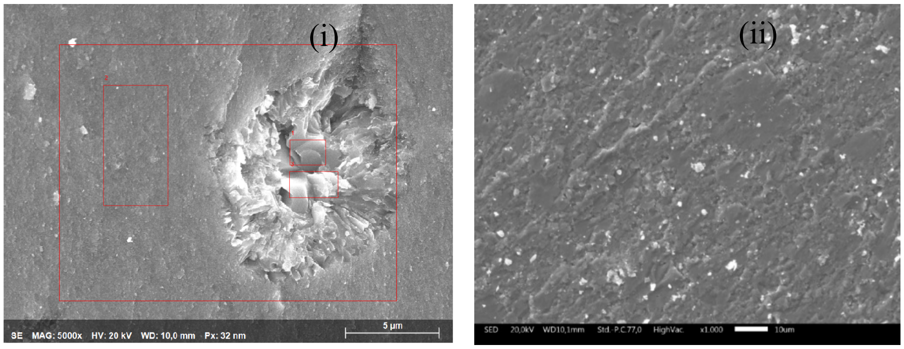

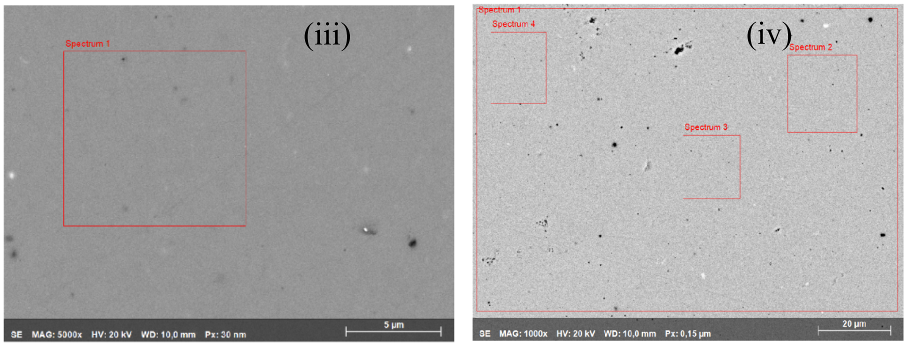

Figure 3. (i) SEM micrograph of the surface of SPS sintered sample A showing compact sample with almost no pores and the presence of SnS.; (ii) WC particles on one of the samples (bright spots in the micrograph, identified by EDX); (iii) micrographs of polished samples A and (iv) B. EDX data are provided in Table S1.

Sample name	Sintering Die	Sintering Pressure (MPa)	Sintering Temperature (°C)	Dwell Time (min)	Density (g/cm^3)	Weight Fraction (±1%)		Average Domain Size (±10 nm)
						Disordered-CTS	Secondary phase name	
A	WC	500	400	60	4.06	99	SnO_2-1	12
B	Graphite	64	512	30	4.52	100		25
C	Graphite	64	500	30	4.45	99	SnO_2-1	37

Table 1. Sample names, sintering conditions, densities, phase purity, and average grain size for various CTS samples.

SEM micrographs on bulk samples reveal a dense microstructure, highly intact grains with almost no porosity (shown in Figure 3, Figure S3, and Figure S4). Unlike the as-milled powder, EDX analysis on the sintered samples revealed a homogeneous chemical distribution, with the exception of sample A, where a small amount of SnS was found, likely due to incomplete reaction at 400 °C (Figure 3i, Figure S3 and S5). Some bright spots in the micrographs revealed traces of WC particles. However, WC and SnS signals were not observed in the XRD patterns because of their small weight fraction, below the detection limit (<<1%). Comparative SEM-EDX analysis was performed on samples A and B (before and after polishing), SEM-EDX data is shown in the supporting information (Figure S3-S6). Sample A has a higher amount of SnS phase compared to sample B, probably due to a lower sintering temperature. However, the matrix composition for both samples is similar, suggesting that stoichiometric deviation in CTS grains is quite small. These micrographs also confirm that the average grain size is much smaller than the magnification of the microscope allows to see.

Figures 4(i) and 4(ii) show the absolute Seebeck coefficient (S) and resistivity (ρ), respectively, for the CTS samples of Table 1. Although there is a variation in the values of S, all the samples show a positive Seebeck coefficient, increasing with temperature. Sample A, B, and C present S ~100 µV/K, 180 µV/K, 160 µV/K, respectively, which is lower than the reported room temperature values for CTS compound (S ~500-700 µV/K).[17,22,27] A general trend of increasing values of Seebeck coefficient with increasing the sintering temperature and grain size can be observed. The Cu-Sn-S systems exist in numerous phases, such as Cu_2SnS_3[16], Cu_3SnS_4[41], $Cu_5Sn_2S_7$[17], and $Cu_7Sn_3S_{10}$[42], etc.[2] Mostly, these systems show *p*-type semiconducting nature due to the unfilled Cu 3*d*-orbitals. Additionally, Cu-S bonds in Cu-Sn-S-based systems form a 3-dimensional conduction network which enhances their electrical conductivity.[15]

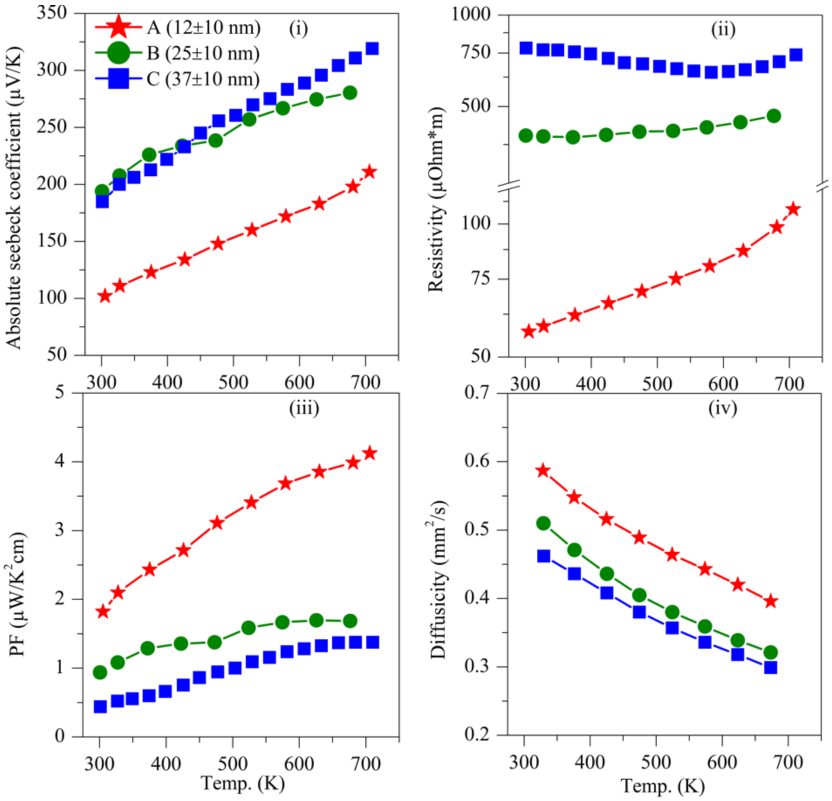

Figure 4. Temperature-dependent (i) absolute Seebeck Coefficient, (ii) Resistivity, (iii) power factor (*PF*), and (iv) diffusivity for sintered samples A, B, and C.

It is well known that undoped CTS is highly resistive with a non-degenerate semiconductor-like trend in temperature owing to its low carrier concentration.[16] However, samples A and B show a degenerate semiconductor-like nature, whereas sample C, with the largest *S* (~320 μV/K, above 650 K), shows a non-degenerate trend up to ~650 K. As expected, samples with a higher Seebeck coefficient have higher electrical resistivity and vice versa, but a trend of decreasing electrical resistivity can also be observed with the decrease in crystalline domain size. It is worth mentioning here that off-stoichiometry in CTS compounds can lead to similar results, although such deviations should have a Cu/Sn ratio >2. In fact, Deng *et al.* [22] show that an excess of Cu in $Cu_{2+x}Sn_{1-x}S_3$ ($x \geq 0.016$) changes the electrical resistivity from a non-degenerate to degenerate behaviour. This suggests that CTS phase, especially when sintered at low *T* (400°C, sample A), is non-stoichiometric.

In general, a small grain size leads to a higher Seebeck coefficient due to the scattering of charge carriers by the grain boundary, otherwise known as Energy-filtering.[43] This, however, decreases the mobility, in turn, increases the electrical resistivity. The lower grain size is also crucial in the suppression of thermal conductivity by scattering phonon waves effectively. The results shown here contrast with the energy filtering mechanism. The samples with smaller domains are more conductive, and we observe a trend of increasing resistivity with an increase in grain size. Carrier concentration measurements on these samples revealed that the higher conductivity of samples with small domains correlates with a higher carrier concentration, 8.6×10^{20} cm^{-3} and 7.4×10^{19} cm^{-3} for samples A and B, respectively. These values are one to two orders of magnitude higher than the reported values for the CTS[27]. However, other Cu-Sn-S based compounds with higher Cu/Sn ratio presented increasing carrier concentration with increasing Cu/Sn ratio, i.e., 2.6×10^{21} cm^{-3} and 5.57×10^{21} cm^{-3} for $Cu_7Sn_3S_{10}$[44] and $Cu_5Sn_2S_7$[17], respectively. Sample A sintered at low sintering temperature has a lower carrier mobility (1.2 cm^2 V^{-1} s^{-1}) than sample B (2.1 cm^2 V^{-1} s^{-1}) which is explained by the larger carrier concentration (increased probability of charge carrier collision) and lower crystallite size in sample A.

Due to the decreased electrical resistivity, sample A shows the highest *PF* values of ~ 4.5 μW/K^2 cm, above 650 K, which is 3-fold and 9-fold higher than cubic (disordered) CTS (*PF* ~1.5 μW/K^2 cm)[27] and monoclinic (ordered) CTS (PF ~0.47 μW/K^2 cm)[15], respectively. Samples B and C have comparatively lower *PF* of ~1.5 μW/K^2 cm and ~1.2 μW/K^2 cm, respectively. The thermal diffusivity measurements are shown in Figure 4(iv). It is evident from the data that samples with smaller domains (more conductive) have a higher diffusivity. From the above considerations, it appears that the electrical properties are strongly dependent on the sintering temperature and grain size. Additional results following the same trend of Seebeck coefficient and electrical resistivity with grain size support this statement (Figure S7). As mentioned above, a slight stoichiometric deviation can occur in the small grains due to the uncomplete reaction and crystallisation at low temperature, leading to high carrier concentration and electrical conductivity. The fast kinetic of reaction and crystallisation during SPS may also lead to variation of compositions at the grain surfaces and boundaries, which could be highly conductive and possibly injecting additional charge carriers in the system.

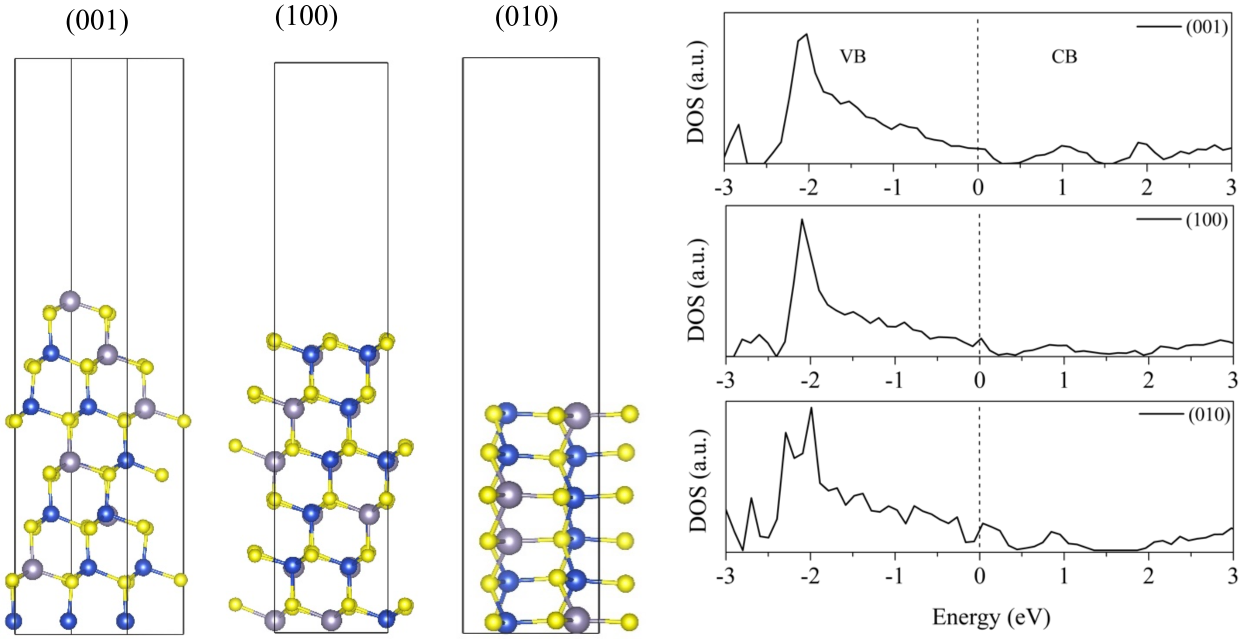

Figure 5. Monoclinic (ordered) CTS slabs with orientation (001), (100), and (010), and corresponding Density of states (DOS) plots. Here, the Fermi level is set to zero. Cu, Sn, and S atoms are represented by blue, grey, yellow colours, respectively.

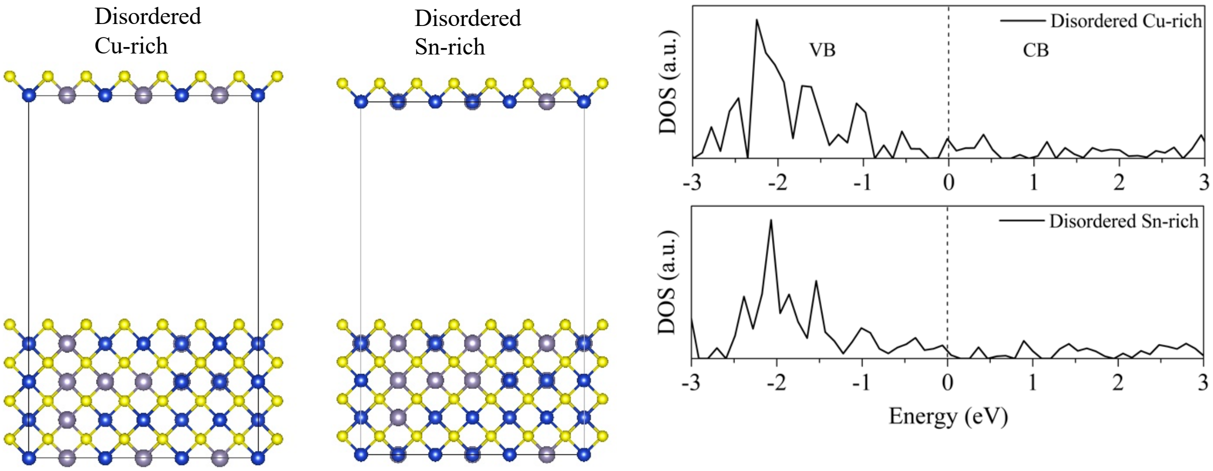

Figure 6. Structures and corresponding Density of states (DOS) for two disordered structures, where one has Cu-rich and other has Sn-rich layer, just below the terminating sulfur layer. Here, the Fermi level is set to zero.

To investigate this further, three ordered and two disordered CTS surfaces (shown in figures 5 and 6, respectively) were studied. The first three images in figure 5 show ordered CTS slabs with (001), (010), and (100) planes. The other two images show disordered structures consisting of a Cu-rich layer and a Sn-rich layer, just below the terminating sulfur layer. Please note that the overall chemistry of CTS system was respected while making all the structures shown in figure 5 and 6. For each structure in figure 5 and figure 6, corresponding DOS are shown with the structures. After minimization, large distortions were observed for the surface atoms of all the structures. The reason is that surface atoms form incomplete bonds due to the change in the coordination number caused by the surface termination. The DOS on the VB side is higher than the CB side showing *p*-type nature. However, no bandgap was observed suggesting a metallic character of all the studied structures. The localized states are visible near the Fermi level due to the dangling bonds on the surface. These dangling bonds provide additional charge carriers (holes), which increase the carrier concentration leading to the degenerate semiconductor-like behaviour observed in Figure 4. We are aware that the calculated structures are not an exact model of the grain boundary effects. Since the grains could terminate with any plane or orientation (favoured by the local environment), these calculations only make plausible the hypothesis that CTS grains should have dangling bonds, which would lead to localized states at the Fermi level and increased electrical conductivity. These results are in agreement with a recent report by Dahule *et al.*[30], although limited to the monoclinic phase.

System	Configuration	Energy of the System	Formation Energy	Formation energy per unit atom
		eV	eV	eV/atom
CTS	24-Cu, 12-Sn, and 36-S	-308.0450	-23.8016	-0.3306
Cu-vacant	23-Cu, 12-Sn, and 36-S	-303.7652	-23.2520	-0.3275
Cu-rich	25-Cu, 11-Sn, and 36-S	-307.5523	-23.42630	-0.3254
Sn-rich	23-Cu, 13-Sn, and 36-S	-306.7465	-22.38570	-0.3109
Sn-vacant	24-Cu, 11-Sn, and 36-S	-302.2878	-21.8920	-0.3083

Table 2. Energy of system, formation energy, and formation energy per unit atom for various CTS systems

Table 2 reports the formation energy per unit atom for vacancy and off stoichiometry in CTS, as obtained from DFT simulations. It is evident from the reported values that after the stoichiometric CTS, Cu-vacant, and Cu-rich systems are energetically more viable, whereas Sn-vacant and Sn-rich systems seem less likely to form. Corresponding DOS plots are shown in the figure S6. Thermodynamically, these conclusions could be generalized to the whole family of Cu-Sn-S systems. In other Cu-Sn-S systems, Cu-vacant and Cu-rich systems would be more likely to form than Sn-rich and Sn-poor phases. Moreover, in this family of materials, Cu vacancy, Cu excess, and Sn vacancy would enable *p*-type doping-like effects, whereas Sn excess showed *n*-type behaviour.

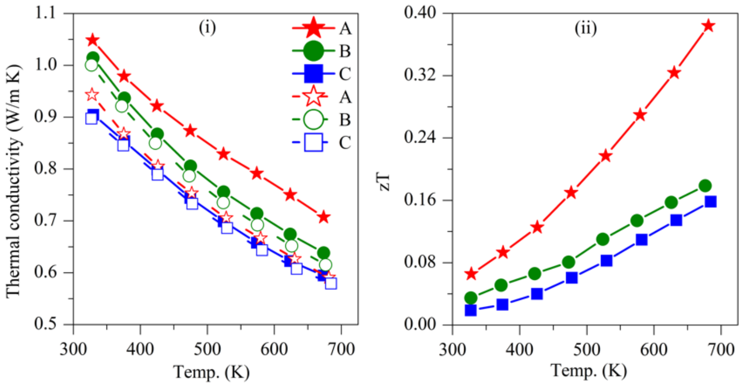

Figure 7. Temperature dependent (i) total thermal conductivity (filled markers connected with solid line) and lattice component of thermal conductivity (empty markers connected with dashed line), and (ii) figure of merit.

The thermal conductivity and figure of merit are shown in Figures 7 (i) and 7 (ii), respectively. Since we are considering the heat capacity well above the Debye temperature (θ_D ~213 K), the total thermal conductivity was calculated considering a constant value of C_p ~0.44 J/g K for all samples. The total thermal conductivity for all samples decreases with temperature, due to an increased phonon-phonon interaction (Umklapp process or *U*-process). The electronic part of thermal conductivity (κ_e) was estimated according to the Wiedemann-Franz law (see equation 3), where the Lorentz number (*L*) was calculated using equation 4[45].

$$L = 1.5 + e^{-\left(\frac{|S|}{116}\right)} \qquad -4$$

where *L* is in 10^{-8} WΩ/K^2 and *S* in μV/K.

It is evident from figure 7(i), at higher temperatures, the lattice part of the thermal conductivity is similar for all the samples, κ_l ~0.6 W/m K, above 673 K. This value is comparatively lower than the diamond-like $CuFeS_{2+x}$. system, where κ_l ~1.0 W/m K is reported at 650 K.[46] However, other Cu-Sn-S based compounds such as Cu_3SnS_4 and Cu_7SnS_{10} show a similar κ_l around 650 K, which further decreases to κ_l ~0.4 W/m K at 750 K.[41,44] The electronic contribution of thermal conductivity is the highest for sample A, and decreases for samples B and C, respectively. This agrees with the corresponding resistivity and carrier concentration measurements, as samples A, B, and C have increasing resistivity (decreasing carrier concentration) in the same order. The figure of merit of samples A, B, and C is equal to 0.40, 0.17, and 0.14 at 673 K, respectively. Overall, the two-step production method can be used to produce high-density nanostructured pellets. The experimental results indicate that a similar zT is reported for $Cu_{2+x}Sn_{1-x}S_3$ systems with Sn substitution ($x = 0.2$) by Zn[15], Ni[18], In[26], etc.

Conclusions:

We have studied the effects of crystalline domain size on the thermoelectric properties using experimental analyses and first-principles simulations. A CTS powder was produced from elemental powders (Cu, Sn, and S) by high-energy reactive ball-milling, subsequently, high-density pellets were produced using spark-plasma-sintering. This method adds a distinct advantage by maintaining the nanostructure while reaching the required high density. Rietveld refinement of the XRD patterns revealed average domain sizes below 50 nm for samples sintered in different conditions. Low temperature SPS sintering of mechanically alloyed powders allows to maintain structural disorder of the CTS phase, while resulting in nanostructured ceramics. This leads to extremely low lattice thermal conductivity. On the other hand, the sample with the smallest average domain size also presents the lowest resistivity and Seebeck coefficient, resulting in the highest power factor. Experimental evidence suggests that S and ρ correlate with the sintering temperature which induces stoichiometric deviations and different grain sizes. First-principles (DFT) simulations of three ordered and two disordered surfaces revealed the presence of dangling bonds and localized states near the Fermi level. DOS at the Fermi level was continuous i.e., bandgap was absent, suggesting that CTS grain boundary is conductive. Formation energies for stoichiometric CTS, Cu-vacant, Cu-rich, Sn-vacant, and Sn-rich CTS are in increasing order, implying stoichiometric CTS is energetically the most favourable, followed by Cu-vacant and Cu-rich systems. The Cu-vacant, Cu-rich, and Sn-vacant systems increase the *p*-type behaviour and carrier concentration, thus explaining the observed low resistivity of the sintered components. Samples with average domain sizes of 12±10 nm, 25±10 nm, and 37±10 nm displayed a figure of merit zT of 0.40, 0.17, and 0.14, respectively, around 673 K. The results presented here for various CTS surfaces, formation energies, and doping effects, can be generalized to a broad family of Cu-Sn-S-based systems. Our synthesis method also provides an interesting route for many materials to synergistically tune their electrical and thermal properties.

Associated content:

Supporting information:

SEM-EDX data on 60-min milled CTS powder.
Rietveld refinement data.
Corresponding EDX data for figure 2.
Comparative SEM-EDX data for unpolished and polished sample A and B.

Temperature dependent absolute Seeebeck coefficient and resistivity for various CTS samples with increasing average domain size.

Density of States (DOS) for Stoichiometric, Cu-vacant, Cu-rich, Sn-vacant, and Sn-rich CTS systems.

Corresponding Author:

Emmanuel Guilmeau
E-mail: emmanuel.guilmeau@ensicaen.fr

Paolo Scardi
E-mail: paolo.scardi@unitn.it

Author Contributions:

Original draft writing: KL & HN; Experimental work: KL, EG, & KM; Computational work: HN;

Editing, proofreading, and discussions: KL, HN, NA, KM, EG, & PS; Conceptualization: EG & PS;

Funding: PS.

Acknowledgement:

The authors are thankful to C. Bilot, J. Lecourt, and Dr. Mirco D'Incau for technical support.

REFERENCES:

(1) Mao, J.; Liu, Z.; Zhou, J.; Zhu, H.; Zhang, Q.; Chen, G.; Ren, Z. Advances in Thermoelectrics. *Advances in Physics* **2018**, *67* (2), 69–147. https://doi.org/10.1080/00018732.2018.1551715.

(2) Jaldurgam, F. F.; Ahmad, Z.; Touati, F. Low-Toxic, Earth-Abundant Nanostructured Materials for Thermoelectric Applications. *Nanomaterials* **2021**, *11* (4), 895. https://doi.org/10.3390/nano11040895.

(3) Wei, T. R.; Qin, Y.; Deng, T.; Song, Q.; Jiang, B.; Liu, R.; Qiu, P.; Shi, X.; Chen, L. Copper Chalcogenide Thermoelectric Materials. *Science China Materials* **2019**, *62* (1), 8–24. https://doi.org/10.1007/s40843-018-9314-5.

(4) Suekuni, K.; Kim, F. S.; Nishiate, H.; Ohta, M.; Tanaka, H. I.; Takabatake, T. High-Performance Thermoelectric Minerals: Colusites Cu 26 V 2 M 6 S 32 (M = Ge, Sn). *Applied Physics Letters* **2014**, *105* (13), 132107. https://doi.org/10.1063/1.4896998.

(5) Guélou, G.; Lemoine, P.; Raveau, B.; Guilmeau, E. Recent Developments in High-Performance Thermoelectric Sulphides: An Overview of the Promising Synthetic Colusites. *Journal of Materials Chemistry C* **2021**, *9* (3), 773–795. https://doi.org/10.1039/D0TC05086E.

(6) Biswas, K.; Zhao, L.-D.; Kanatzidis, M. G. Tellurium-Free Thermoelectric: The Anisotropic n-Type Semiconductor Bi2S3. *Advanced Energy Materials* **2012**, *2* (6), 634–638. https://doi.org/10.1002/aenm.201100775.

(7) Tan, G.; Hao, S.; Zhao, J.; Wolverton, C.; Kanatzidis, M. G. High Thermoelectric Performance in Electron-Doped AgBi 3 S 5 with Ultralow Thermal Conductivity. *Journal of the American Chemical Society* **2017**, *139* (18), 6467–6473. https://doi.org/10.1021/jacs.7b02399.

(8) Zhai, H.; Xiao, Y.; Zhao, L.-D.; Tan, G.; Tang, X. Large Effective Mass and Low Lattice Thermal Conductivity Contributing to High Thermoelectric Performance of Zn-Doped Cu5Sn2Se7. *Journal of Alloys and Compounds* **2020**, *826*, 154154. https://doi.org/10.1016/j.jallcom.2020.154154.

(9) Powell, A. V. Recent Developments in Earth-Abundant Copper-Sulfide Thermoelectric Materials. *Journal of Applied Physics* **2019**, *126* (10), 100901. https://doi.org/10.1063/1.5119345.

(10) Baláž, P.; Achimovičová, M.; Baláž, M.; Chen, K.; Dobrozhan, O.; Guilmeau, E.; Hejtmánek, J.; Knížek, K.; Kubíčková, L.; Levinský, P.; Puchý, V.; Reece, M. J.; Varga, P.; Zhang, R. Thermoelectric Cu–S-Based Materials Synthesized via a Scalable Mechanochemical Process. *ACS Sustainable Chemistry & Engineering* **2021**, *9* (5), 2003–2016. https://doi.org/10.1021/acssuschemeng.0c05555.

(11) Snyder, G. J.; Toberer, E. S. Complex Thermoelectric Materials. *Nature Materials* **2008**, *7* (February), 105–114. https://doi.org/10.1038/nmat2090.

(12) Beretta, D.; Neophytou, N.; Hodges, J. M.; Kanatzidis, M. G.; Narducci, D.; Martin-Gonzalez, M.; Beekman, M.; Balke, B.; Cerretti, G.; Tremel, W.; Zevalkink, A.; Hofmann, A. I.; Müller, C.; Dörling, B.; Campoy-Quiles, M.; Caironi, M. Thermoelectrics: From History, a Window to the Future. *Materials Science and Engineering R: Reports* **2018**, *138* (November 2018), 210–255. https://doi.org/10.1016/j.mser.2018.09.001.

(13) Zhang, X.; Bu, Z.; Shi, X.; Chen, Z.; Lin, S.; Shan, B.; Wood, M.; Snyder, A. H.; Chen, L.; Snyder, G. J.; Pei, Y. Electronic Quality Factor for Thermoelectrics. *Science advances* **2020**, *6* (46), eabc0726. https://doi.org/10.1126/sciadv.abc0726.

(14) Dias, S.; Kumawat, K.; Biswas, S.; Krupanidhi, S. B. Solvothermal Synthesis of Cu 2 SnS 3 Quantum Dots and Their Application in Near-Infrared Photodetectors. *Inorganic Chemistry* **2017**, *56* (4), 2198–2203. https://doi.org/10.1021/acs.inorgchem.6b02832.

(15) Shen, Y.; Li, C.; Huang, R.; Tian, R.; Ye, Y.; Pan, L.; Koumoto, K.; Zhang, R.; Wan, C.; Wang, Y. Eco-Friendly p-Type Cu2SnS3 Thermoelectric Material: Crystal Structure and Transport Properties. *Scientific Reports* **2016**, *6* (1), 32501. https://doi.org/10.1038/srep32501.

(16) Lohani, K.; Isotta, E.; Ataollahi, N.; Fanciulli, C.; Chiappini, A.; Scardi, P. Ultra-Low Thermal Conductivity and Improved Thermoelectric Performance in Disordered Nanostructured Copper Tin Sulphide (Cu2SnS3, CTS). *Journal of Alloys and Compounds* **2020**, *830* (C), 154604. https://doi.org/10.1016/j.jallcom.2020.154604.

(17) Pavan Kumar, V.; Lemoine, P.; Carnevali, V.; Guélou, G.; Lebedev, O. I.; Boullay, P.; Raveau, B.; Al Rahal Al Orabi, R.; Fornari, M.; Prestipino, C.; Menut, D.; Candolfi, C.; Malaman, B.; Juraszek, J.; Guilmeau, E. Ordered Sphalerite Derivative Cu 5 Sn 2 S 7 : A Degenerate Semiconductor with High Carrier Mobility in the Cu–Sn–S Diagram. *Journal of Materials Chemistry A* **2021**, *9* (17), 10812–10826. https://doi.org/10.1039/D1TA01615F.

(18) Xu, X.; Zhao, H.; Hu, X.; Pan, L.; Chen, C.; Li, D.; Wang, Y. Synergistic Role of Ni-Doping in Electrical and Phonon Transport Properties of Cu2Sn1-XNixS3. *Journal of Alloys and Compounds* **2017**, *728*, 701–708. https://doi.org/10.1016/j.jallcom.2017.08.227.

(19) Zhai, Y.-T.; Chen, S.; Yang, J.-H.; Xiang, H.-J.; Gong, X.-G.; Walsh, A.; Kang, J.; Wei, S.-H. Structural Diversity and Electronic Properties of Cu2SnX3 (X=S, Se): A First-Principles Investigation. *Physical Review B* **2011**, *84* (7), 075213. https://doi.org/10.1103/PhysRevB.84.075213.

(20) Shigemi, A.; Maeda, T.; Wada, T. First-Principles Calculation of Cu2SnS3 and Related Compounds. *Physica Status Solidi (B) Basic Research* **2015**, *252* (6), 1230–1234. https://doi.org/10.1002/pssb.201400346.

(21) Zhao, H.; Xu, X.; Li, C.; Tian, R.; Zhang, R.; Huang, R.; Lyu, Y.; Li, D.; Hu, X.; Pan, L.; Wang, Y. Cobalt-Doping in Cu2SnS3: Enhanced Thermoelectric Performance by Synergy of Phase Transition and Band Structure Modification. *Journal of Materials Chemistry A* **2017**, *5* (44), 23267–23275. https://doi.org/10.1039/c7ta07140j.

(22) Deng, T.; Qiu, P.; Song, Q.; Chen, H.; Wei, T.-R.; Xi, L.; Shi, X.; Chen, L. Thermoelectric Properties of Non-Stoichiometric Cu2+ XSn1− XS3 Compounds. *Journal of Applied Physics* **2019**, *126* (8), 085111. https://doi.org/10.1063/1.5115195.

(23) Zhao, L.; Chen, C.; Pan, L.; Hu, X.; Lu, C.; Wang, Y. Magnetic Iron Doping in Cu 2 SnS 3 Ceramics for Enhanced Thermoelectric Transport Properties. *Journal of Applied Physics* **2019**, *125* (9), 095107. https://doi.org/10.1063/1.5065074.

(24) Zhang, Z.; Zhao, H.; Wang, Y.; Hu, X.; Lyu, Y.; Cheng, C.; Pan, L.; Lu, C. Role of Crystal Transformation on the Enhanced Thermoelectric Performance in Mn-Doped Cu2SnS3. *Journal of Alloys and Compounds* **2019**, *780*, 618–625. https://doi.org/10.1016/j.jallcom.2018.11.329.

(25) Aihara, N.; Matsumoto, Y.; Tanaka, K. Exciton Luminescence from Cu 2 SnS 3 Bulk Crystals. *Applied Physics Letters* **2016**, *108* (9), 092107. https://doi.org/10.1063/1.4943229.

(26) Tan, Q.; Sun, W.; Li, Z.; Li, J. F. Enhanced Thermoelectric Properties of Earth-Abundant Cu2SnS3 via In Doping Effect. *Journal of Alloys and Compounds* **2016**, *672*, 558–563. https://doi.org/10.1016/j.jallcom.2016.02.185.

(27) Lohani, K.; Nautiyal, H.; Ataollahi, N.; Fanciulli, C.; Sergueev, I.; Etter, M.; Scardi, P. Experimental and Ab Initio Study of Cu 2 SnS 3 (CTS) Polymorphs for Thermoelectric Applications. *The Journal of Physical Chemistry C* **2021**, *125* (1), 178–188. https://doi.org/10.1021/acs.jpcc.0c09139.

(28) Siyar, M.; Cho, J. Y.; Youn, Y.; Han, S.; Kim, M.; Bae, S. H.; Park, C. Effect of Annealing Temperature on the Phase Transition, Band Gap and Thermoelectric Properties of Cu2SnSe3. *Journal of Materials Chemistry C* **2018**, *6* (7), 1780–1788. https://doi.org/10.1039/c7tc05180h.

(29) Baranowski, L. L.; McLaughlin, K.; Zawadzki, P.; Lany, S.; Norman, A.; Hempel, H.; Eichberger, R.; Unold, T.; Toberer, E. S.; Zakutayev, A. Effects of Disorder on Carrier Transport in Cu2SnS3. *Physical Review Applied* **2015**, *4* (4), 044017. https://doi.org/10.1103/PhysRevApplied.4.044017.

(30) Dahule, R.; Raghav, A.; Hanindriyo, A. T.; Hongo, K.; Maezono, R.; Panda, E. Surface Study of Cu 2 SnS 3 Using First-Principles Density Functional Theory. *Advanced Theory and Simulations* **2021**, *4* (6), 2000315. https://doi.org/10.1002/adts.202000315.

(31) Baláž, P.; Dutková, E.; Levinský, P.; Daneu, N.; Kubíčková, L.; Knížek, K.; Baláž, M.; Navrátil, J.; Kašparová, J.; Ksenofontov, V.; Möller, A.; Hejtmánek, J. Enhanced Thermoelectric Performance of Chalcopyrite Nanocomposite via Co-Milling of Synthetic and Natural Minerals.

Materials Letters **2020**, *275* (June), 128107. https://doi.org/10.1016/j.matlet.2020.128107.

(32) Kresse, G.; Furthmüller, J. Efficient Iterative Schemes for Ab Initio Total-Energy Calculations Using a Plane-Wave Basis Set. *Physical Review B - Condensed Matter and Materials Physics* **1996**, *54* (16), 11169–11186. https://doi.org/10.1103/PhysRevB.54.11169.

(33) Kresse, G.; Furthmüller, J. Efficiency of Ab-Initio Total Energy Calculations for Metals and Semiconductors Using a Plane-Wave Basis Set. *Computational Materials Science* **1996**, *6* (1), 15–50. https://doi.org/10.1016/0927-0256(96)00008-0.

(34) Perdew, J. P.; Burke, K.; Ernzerhof, M. Generalized Gradient Approximation Made Simple. *Physical Review Letters* **1996**, *77* (18), 3865–3868. https://doi.org/10.1103/PhysRevLett.77.3865.

(35) Pack, J. D.; Monkhorst, H. J. “special Points for Brillouin-Zone Integrations”-a Reply. *Physical Review B* **1977**, *16* (4), 1748–1749. https://doi.org/10.1103/PhysRevB.16.1748.

(36) Scardi, P.; Leoni, M. Diffraction Line Profiles from Polydisperse Crystalline Systems. *Acta Crystallographica Section A: Foundations of Crystallography* **2001**, *57* (5), 604–613. https://doi.org/10.1107/S0108767301008881.

(37) Coelho, A. A. TOPAS and TOPAS-Academic: An Optimization Program Integrating Computer Algebra and Crystallographic Objects Written in C++. *Journal of Applied Crystallography* **2018**, *51* (1), 210–218. https://doi.org/10.1107/S1600576718000183.

(38) Scardi, P.; Azanza Ricardo, C. L.; Perez-Demydenko, C.; Coelho, A. A. Whole Powder Pattern Modelling Macros for TOPAS. *Journal of Applied Crystallography* **2018**, *51* (6), 1752–1765. https://doi.org/10.1107/s160057671801289x.

(39) Black, D. R.; Mendenhall, M. H.; Brown, C. M.; Henins, A.; Filliben, J.; Cline, J. P. Certification of Standard Reference Material 660c for Powder Diffraction. *Powder Diffraction* **2020**, *35* (1), 17–22. https://doi.org/10.1017/S0885715620000068.

(40) McCusker, L. B.; Von Dreele, R. B.; Cox, D. E.; Louër, D.; Scardi, P. Rietveld Refinement Guidelines. *Journal of Applied Crystallography* **1999**, *32* (1), 36–50. https://doi.org/10.1107/S0021889898009856.

(41) Yang, Y.; Ying, P.; Wang, J.; Liu, X.; Du, Z.; Chao, Y.; Cui, J. Enhancing the Thermoelectric Performance of Cu 3 SnS 4 -Based Solid Solutions through Coordination of the Seebeck Coefficient and Carrier Concentration. *Journal of Materials Chemistry A* **2017**, *5* (35), 18808–18815. https://doi.org/10.1039/C7TA05253G.

(42) Deng, T.; Qiu, P.; Xing, T.; Zhou, Z.; Wei, T. R.; Ren, D.; Xiao, J.; Shi, X.; Chen, L. A Low-Cost and Eco-Friendly Br-Doped Cu7Sn3S10thermoelectric Compound WithzTaround Unity. *Journal of Materials Chemistry A* **2021**, *9* (12), 7946–7954. https://doi.org/10.1039/d0ta12042a.

(43) Narducci, D.; Selezneva, E.; Cerofolini, G.; Frabboni, S.; Ottaviani, G. Impact of Energy Filtering and Carrier Localization on the Thermoelectric Properties of Granular Semiconductors. *Journal of Solid State Chemistry* **2012**, *193*, 19–25. https://doi.org/10.1016/j.jssc.2012.03.032.

(44) Deng, T.; Qiu, P.; Xing, T.; Zhou, Z.; Wei, T.-R.; Ren, D.; Xiao, J.; Shi, X.; Chen, L. A Low-Cost and Eco-Friendly Br-Doped Cu 7 Sn 3 S 10 Thermoelectric Compound with ZT around Unity. *Journal of Materials Chemistry A* **2021**, *9* (12), 7946–7954. https://doi.org/10.1039/D0TA12042A.

(45) Kim, H.-S.; Gibbs, Z. M.; Tang, Y.; Wang, H.; Snyder, G. J. Characterization of Lorenz Number

with Seebeck Coefficient Measurement. *APL Materials* **2015**, *3* (4), 041506. https://doi.org/10.1063/1.4908244.

(46) Xie, H.; Su, X.; Yan, Y.; Liu, W.; Chen, L.; Fu, J.; Yang, J.; Uher, C.; Tang, X. Thermoelectric Performance of CuFeS2+2x Composites Prepared by Rapid Thermal Explosion. *NPG Asia Materials* **2017**, *9* (6), e390–e390. https://doi.org/10.1038/am.2017.80.

TOC:

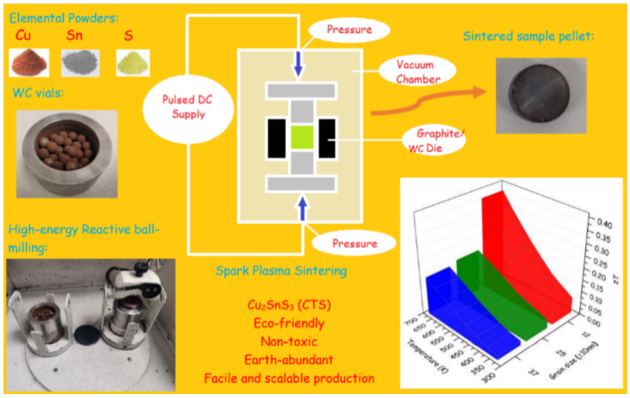
Elemental Powders:
Cu
Sn
S
WC vials:
High-energy Reactive ball-milling:
Pulsed DC Supply
Pressure
Vacuum Chamber
Graphite/ WC Die
Pressure
Spark Plasma Sintering
Sintered sample pellet:
Cu_2SnS_3 (CTS)
Eco-friendly
Non-toxic
Earth-abundant
Facile and scalable production
0.40
0.35
0.30
0.25
0.20
0.15
0.10
0.05
0.00
zT
700
650
600
550
500
450
400
350
300
Temperature (K)
37
15
11
Grain size (±10nm)